JCAMECH

Vol. 50, No. 2, December 2019, pp 387-394
DOI: 10.22059/jcamech.2019.291082.440

Numerical simulation of the fluid dynamics in a 3D spherical model of partially liquefied vitreous due to eye movements under planar interface conditions

Javad Bayat[a], Homayoun Emdad[a] and Omid Abouali [a,]*

[a] *School of mechanical Engineering, Shiraz University, Shiraz, Iran*

ARTICLE INFO

Article history:
Received: 20 October 2019
Accepted: 12 December 2019

Keywords:
Two-phase flow
Viscoelastic-Newtonian fluid
Partial vitreous liquefaction
Harmonic motion
Vitreous

ABSTRACT

Partially liquefied vitreous humor is a common physical and biochemical degenerative change in vitreous body which the liquid component gets separated from collagen fiber network and leads to form a region of liquefaction. The main objective of this research is to investigate how the oscillatory motions influence flow dynamics of partial vitreous liquefaction (PVL). So far computational fluid dynamics modeling of the PVL has not yet been well studied. To this end, a spherical model of the vitreous is subjected to harmonic motion and the numerical simulations are performed for various planar interface conditions in linear viscoelastic regimes. A numerical solver is developed in the OpenFOAM toolbox which is based on finite volume method and uses the PIMPLE algorithm and the dynamic mesh technique. This solver also uses modified classic volume-of-fluid approach to capture the interface effects and dynamic characteristics of two-phase viscoelastic-Newtonian fluid flow. The numerical model is validated by comparing the obtained results with the analytical solution which excellent agreement was observed. The results showed that the intensity of secondary flow in the vertical direction was much higher for the PVL with a higher liquefied fraction. Also, the obtained maximum stresses were dependent on the liquefied fraction of the PVL and located on the equatorial plane at the cavity wall near the interface layer and within the vitreous gel.

1. Introduction

The normal human eye is an isolated sensory organ with a slightly irregular hollow sphere that reacts to light and allows vision. The largest volume of posterior eyeball bounded by the posterior lens curvature, the ciliary body and retina tissue is filled with vitreous containing 98-99% water and salts, sugars, highly swollen of collagen (protein fibers) and hyaluronic acid as the remaining volume [1, 2]. It has been demonstrated by previous researchers that these components provide a highly hydrated gel-like structure with viscoelastic behavior for normal vitreous [3-9]. Physical and biochemical changes in the vitreous occur with age, such as vitreous liquefaction (synchysis) and fiber aggregation (syneresis) which are important in the pathogenesis of many vitreoretinal diseases. The vitreous liquefaction leads to formation of the pockets of liquid known as lacunae. In this biological phenomenon, liquid get separated from collagen, gradually enlarges and coalesces within the vitreous [10, 11].

Balazs and Flood [12] reported the existence of the vitreous liquefaction in the eyes of a 4-year-old baby, and also showed that 20 percent of the posterior eyeball volume in teenagers undergoes liquefaction. Balazs and Denlinger [13] examined the impact of aging on the human eye's vitreous. Their evidences indicate that more than half of the vitreous body is liquefied in ages ranging from 80 to 90 years. Lee et al. [3] showed that aging has a significant impact on the loss of elasticity of the gel in the eyeball cavity and the amount of liquefaction is considerable with increase of age. Nowadays, ophthalmologists and researchers believe that vitreous liquefaction can be considered as the main reason of many ocular disorders such as retinal tears, retinal detachment, vitreomacular traction (VMT), macular pucker, macular hole and etc. [14, 15]. The effect of eye movement on the PVL is quite complex and its understanding is important and to our knowledge has not been addressed so far, from a mechanical point of view, even in a simple configuration in the literature. David et al. [16] analytically assessed the saccadic motion of linear viscoelastic fluid based on experimental data provided by Lee et al. [3] and also studied Newtonian fluid flow numerically inside the spherical geometry. Lee et al. [17] analytically studied the viscoelastic flow field between two concentric spheres and presented the effects of radius and Deborah number in addition to secondary flows. Meskauskas et al. [18] mathematically calculated the stress exerted on the wall boundary of a rigid sphere filled with vitreous humor as a viscoelastic fluid during oscillatory motions. They showed that due to resonant excitation of vitreous motion, the maximum value of velocity occurs inside the domain and can be more than

* Corresponding author. Tel.: +98-713-613-3034; fax: +98-713-647-3511; e-mail: abouali@shirazu.ac.ir

twice of that for the wall boundary. Repetto et al. [19] numerically simulated the dynamics of the detached vitreous due to saccadic eye movements using Comsol Multiphysics. They tested the various posterior vitreous detachment configurations and reported the tractions exerted on the retina. Abouali et al. [20] investigated the liquefied vitreous flow dynamics due to saccadic eye movement. Their results had good agreement with analytical solution obtained from David et al. [16] for a spherical cavity. Modareszadeh and Abouali [21] simulated the effects of sinusoidal motions on the flow dynamics of human vitreous humor as a viscoelastic substance in linear and non-linear regime for different 2D and 3D geometries. They showed, for the same angular frequency and amplitude in the linear regime, the maximum value of wall shear stress for the vitreous chamber filled with the vitreous gel is about 10 times of that for the one filled with fully liquefied vitreous.

The literature survey reveals the lack of numerical analysis for simulating the effects of human eye movements on dynamic characteristics of the PVL. The aim of this paper is to develop a 3D numerical solver for two-phase viscoelastic-Newtonian fluids to assess this important application in biofluid mechanics. In the present study, for the first time, various planar interface conditions with initial circular shape are investigated in a simple three-dimensional model of vitreous chamber subjected to sinusoidal rotations. The paper is outlined as follows. In section 2, the computational model is described. The methodology and numerical approaches are presented in section 3. The results and discussion are explained in section 4. Finally, the conclusions from this study are presented in section 5.

2. Model description

The PVL configuration inside a sphere cavity with Ro equal to 12.5 mm (the radius of human vitreous chamber) is illustrated in Fig. 1. This configuration is selected based on previous experimental and clinical observations for one of the possible PVL shapes. It has been shown that vitreous liquefaction usually originates from the central portion of the vitreous (as early liquefaction) and in the next, the pockets of liquid gradually coalesce, and eventually, the enlarged liquefied region can lead to separation of the posterior vitreous from the retina. This is due to the physiological weakening of vitro-retinal adhesion between vitreous and inner layer of the retina especially in the posterior segment of the eye. In this process, gel-like vitreous falls into the one part of the chamber and the cavity is filled with two-phase viscoelastic-Newtonian fluid (Fig. 1, as posterior vitreous detachment) [22-26]. As depicted, the PVL contains two regions: one is liquefied vitreous assumed as a Newtonian fluid (purely viscous fluid), and the other is vitreous gel with viscoelastic properties occupying the rest of domain. Fig. 1 shows a planar interface condition with the initial circular shape for the PVL which different values are set for $h/2R_o$ ratios in the present study.

2.1. Vitreous rheology

In order to model the gel-like behavior of vitreous, the measured dynamic moduli of vitreous humor available in the literature are considered. Bonfiglio et al. [9] prepared an artificial vitreous which had viscoelastic properties similar to real vitreous humor following the instructions presented by Kummer et al. [27]. They reported values of the complex modulus with respect to angular frequency for five different solutions (s1-s5) with various concentrations of agar powder and hyaluronic acid sodium salt mixed in deionised water. Among their experimental data, the rheological properties of solution s5 are selected for this study. To cover a wide range of shear rates a three-mode Giesekus model was applied since the capability of this model has been confirmed in shearing flows [28]. Therefore, the best fits for dynamic moduli, relaxation time and mobility factor (shown in Table 1) were obtained by a rheometric software named RheoChart. This software is utilized to optimize the behavior of a differential viscoelastic model by using a proper algorithm to analyze the rheological data. It should be noted that since there were significant differences among experimental data and one and two-mode Giesekus models [29], hence, 3-mode type of this model was tested in present work and excellent agreements between experimental data and the results of 3-mode Giesekus model were observed.

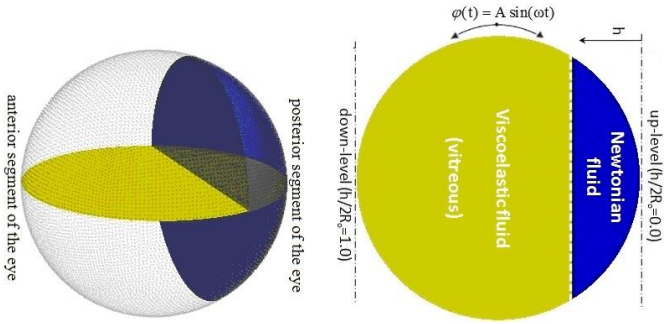

(a) (b) equatorial plane

Figure 1. A simple computational model of the partial vitreous liquefaction with a planar interface. Gel and liquefied vitreous regions are shown in yellow and blue, respectively; (a) the computational model of the PVL, and (b) cross section along the equatorial plane of the model.

Table 1. Parameters of the 3-mode Giesekus viscoelastic model. The G, λ, α, η_p and η_s, respectively, denote dynamic modulus, relaxation time, mobility factor, solvent viscosity and polymer viscosity [28, 29]

Mode	G [Pa]	λ [s]	α	η_p [Pa.s]	η_s [Pa.s]
1	8.88882	0.01576	0.10954	0.14009	0.001
2	6.16848	3.00229	0.56796	18.51959	0.001
3	2.95193	0.10996	0.74892	0.32460	0.001

3. Methodology and Numerical Approaches

The governing equations of the PVL flow as a two-phase viscoelastic-Newtonian fluid flow in each viscoelastic mode are continuity, momentum and constitutive relation. For the Giesekus model [29] the constitutive relation is shown in Eq. (1)). These governing equations are solved numerically and the dynamic mesh technique was used to model the eye movement [21].

$$\tau_{p,n} + \lambda_n \overset{\nabla}{\tau}_{p,n} + \alpha_n \frac{\lambda_n}{\eta_{p,n}} \left(\tau_{p,n} . \tau_{p,n} \right) = \eta_{p,n} \left[\nabla u + \left(\nabla u \right)^T \right] \tag{1}$$

where τ and u are the polymeric stress tensor and fluid velocity, respectively. Also, n is viscoelastic mode index and ∇ denotes the upper convected derivative [21, 29]. Furthermore, the VOF methodology (Hirt and Nicols [30]) is used to track the two-phase flow interface. In this method the following transport

equation for a scalar function (with values in the range of [0, 1]) is being solved:

$$\frac{\partial \gamma}{\partial t} + \nabla.\left[\gamma\left(u - u_g\right)\right] + \nabla.\left[U_r\left(\gamma(1-\gamma)\right)\right] = 0 \quad (2)$$

Here u_g indicates the cell velocity vector of moving mesh and U_r is the artificial compressive velocity to limit numerical diffusion and the interface smear [31]. In this strategy, the $\gamma(1-\gamma)$ scaling ensures that the artificial velocity only acts in the perpendicular direction of the interface [32, 33]. Also, the flow of the PVL is laminar, incompressible, isothermal, and the density of both phases (vitreous gel and liquefied vitreous region) is considered equal to 1000 kg/m^3. In this paper, in an open source CFD toolbox called OpenFOAM [34], a generic numerical solver is developed in order to simulate the different cases involving two-phase viscoelastic-Newtonian fluids. The time-dependent sets of coupled non-linear partial differential equations have been discretized using the finite volume technique [35, 36]. The PIMPLE procedure has been applied for the pressure-velocity coupling which is a combination of SIMPLE and PISO algorithms [37-39]. Fig. 2 presents the flowchart of the computation steps for two-phase viscoelastic-Newtonian fluid flows used in this work. Different types of discretization schemes were tested to employ proper schemes for spatial derivatives, since an unsuitable choice may lead to instability and oscillation in the solution. In this study, second order accuracy is considered for discretization of all gradient and Laplacian terms and the convective terms are discretized by utilizing the Normalized Variation Diminishing scheme [40]. Moreover, the second-order implicit backward method is used for time derivatives. In terms of the linear system solver, according to Ajiz and Jennings [41] and Lee et al. [42], preconditioned conjugate gradient method (PCG) combined with AMG (Algebraic multi-grid method) preconditioning is used for pressure terms. Also, BiCGstab (Bi-conjugate gradient stabilized) method with DILU (Diagonal incomplete lower-upper) preconditioning is applied for velocity and stress terms in both single and multimode cases. Absolute tolerances have been set 10^{-9} for the residuals of the velocity, pressure and stress quantities in numerical solutions. When the retardation ratio (the viscosity ratio of the two-phases) approaches zero, the elliptic diffusion term in momentum equation becomes small and this might lead to instability in numerical solution [43]. As a result, in this research we utilized the discrete elastic split stress (DEVSS) method proposed by Guénette and Fortin [44] to enhance the stability of numerical solution. In this method, an artificial diffusion is introduced to the right and left side of momentum equation explicitly and implicitly, respectively in order to increase the elliptical characteristic of this equation. The no-slip boundary condition is set for the wall cavity which means the fluid adjacent to the wall has the same velocity as the wall. The sinusoidal oscillation for the eye starts from the initial condition to the left up to its maximum amplitude which is followed by a return movement to its maximum amplitude in the right direction. Subsequently, cavity changes the direction of motion and returns to its initial position. It should be noted that the numerical solution is continued until the flow field reaches the periodic state. Thus in this periodic torsional oscillation, the angular displacement of the sphere with respect to time is applied by the following time law:

$$\varphi(t) = A\sin(\omega t) \quad (3)$$

where A and ω represent the amplitude and frequency of rotation about a normal axis passing through the centre of equatorial plane.

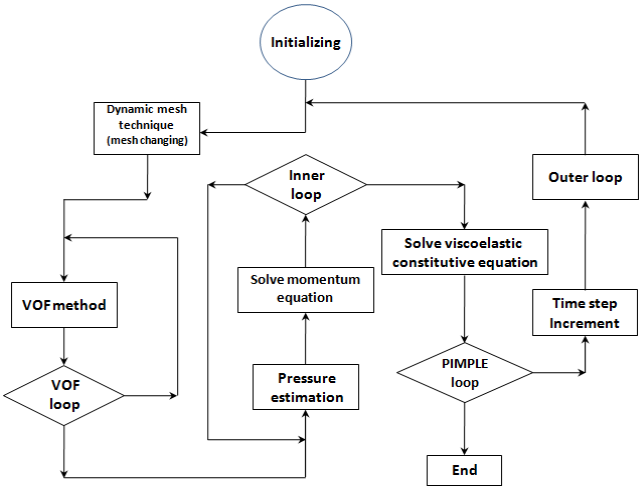

Figure 2. Flowchart of the computational steps

A structured 3-D numerical mesh was generated for numerical model of the vitreous cavity. The computational domain was divided into 7 zones. Each zone was meshed as a topological cube. The generated mesh in equatorial plane is a combination of O-type and H-type grids. In order to confirm grid-independency of the results, several tests were performed. Table 2 depicts the numerical results of different parameters for the PVL with volume fraction of $h/2R_o=0.5$ obtained for the angular frequency of 10 rad/sec and amplitude of 0.3 rad. Since present numerical simulations showed that the dependence of the results to the mesh size for stress terms is higher compared with that for the velocity values (not reported here for sake of brevity), thus the grid independence check was performed by calculating the maximum shear stress ($\tau_{r\theta}$) and maximum first normal stress difference ($N_1=\tau_{\theta\theta}-\tau_{rr}$) and the results are shown in Table 2. The relative differences in these two parameters (columns 2 and 3 in Table 2) between medium and fine meshes are less than 3% and 4%, respectively. Hence, the grid with 1,578,352 computational cells was chosen for other numerical runs.

Notably, the selected grid was also enough and accurate to provide the excellent agreements between numerical results and presented analytical solutions (Appendix 1) for variations of tangential velocity magnitude and shear stress magnitude (Figs. A2a and A2b in the concentric PVL configurations).

Table 2 The grid independency check for the computational domain with $h/2R_o=0.5$ at A=0.3 rad and ω=10 rad/sec

Mesh cases	maximum $\tau_{r\theta}$ (Pa)	maximum N_1 (Pa)
764,544	2.72	4.45
1,578,352	3.33	5.50
1,853,182	3.42	5.71

Also, for finding the optimum computational time, several tests with different time-step values were carried out. Eventually, time-step equal to 0.25 ms was applied for all simulations.

4. Results and discussion

As there is no available experimental data or analytical solution for a two-phase Newtonian-viscoelastic flow with the planar interface, the validation has been performed for a case with concentric PVL configuration. The validation is presented in the appendix for the periodic motions of a concentric PVL

configuration with different volume fractions (Fig. A1) in comparison with the analytical solution. After validation of present numerical model, now the obtained results and corresponding discussions for various planar interface conditions with initial circular shape (Fig. 1) are presented in this section. Fig. 3 shows the variations of the normalized tangential velocity with respect to radial direction of cavity across the interface layer at time equal to T for different $h/2R_o$ ratios. This figure is obtained for angular frequency of 10 rad/sec, amplitude of 0.03 rad and each curve is scaled with its maximum value during the motion. For $h/2R_o$ ratio equal to 0.0 (normal vitreous humor) and in the viscoelastic regions of partially liquefied vitreous humor, tangential velocities vary almost linearly (like rigid body motion) while for fully liquefied vitreous ($h/2R_o$=1.0), a thin boundary layer is formed near the wall leading to formation of a sharp velocity gradient. This slope across the interface decreases slightly by decreasing the $h/2R_o$ ratio. Also, the results depict that for higher $h/2R_o$ ratios, the velocity gradient inside the lacunae is lower. From the figure, the boundary layer thickness for fully liquefied vitreous is less than 1.25 mm and tangential velocity becomes near to the stagnant condition close to the center of cavity. While for lower $h/2R_o$ ratios, with an increase in the kinematic viscosity due to the presence of the vitreous gel, the amount of flow propagation to the center of cavity is increased and the induced force on the wall boundary is felt with entire domain. Therefore, this figure demonstrates the dependency of velocity field in the vitreous on volume fraction of liquefied region. Moreover, the values of non-dimensional parameters including the Reynolds numbers ($2uR_o/\upsilon$ and $2uR_o/\upsilon^*$, where υ and υ^* are kinematic viscosity of purely viscous fluid and complex kinematic viscosity of viscoelastic fluid) and the Weissenberg number (λu) of vitreous, which are calculated based on the maximum velocity in a period, are equal to 93.75, 0.67 and 0.01, respectively.

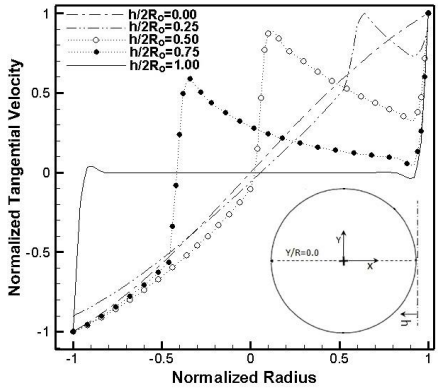

Figure 3. Variations of the normalized tangential velocity across the interface (along X direction on the Y/R=0.0 line), scaled with the maximum tangential velocity at t=T in different h/2Ro ratios for angular frequency of 10 rad/sec and amplitude of 0.03 rad.

The time variations of the maximum shear stress ($\tau_{r\theta}$) and first normal stress difference N_1 during one period of motion for various $h/2R_o$ ratios are obtained and shown in Figs. 4a and 4b, respectively. As the figure depicts, for $h/2R_o$ ratio up to 0.5, stresses increase by increasing $h/2R_o$ ratio and after that these two parameters have a decreasing trend with the increment of $h/2R_o$ from 0.5 to 1.0. In other words, the stresses have a strong dependence on the volume fraction of lacunae and our numerical simulation indicates that the peaks of stresses occur at $h/2R_o$=0.5 where the radius of planar circular interface is maximum in the sphere. For instance, with fifty percent increment of $h/2R_o$ from 0.25 to 0.5, the maximum shear stress and first normal stress difference increase 20% and 14% at t=0.25T (the time of change in direction of oscillatory motion and abrupt variation of the acceleration), respectively. Interestingly, for $h/2R_o$ ratios equal to 0.25, 0.5 and 0.75, the normal stress plays an important role on flow dynamics of the PVL and also, the first normal stress difference becomes higher than the shear stress so that for $h/2R_o$=0.5, the percentage increase is almost 40%. Also, it is observed from Fig. 4 that, a healthy vitreous gel ($h/2R_o$=0.0) cannot generate the remarkable normal stress difference and its maximum N_1 is negligible in comparison with the maximum shear stress. Similarly, by increasing of $h/2R_o$ ratio more than 0.75, the importance of N_1 is sharply reduced and finally in full liquefied vitreous humor its value reaches zero as expected.

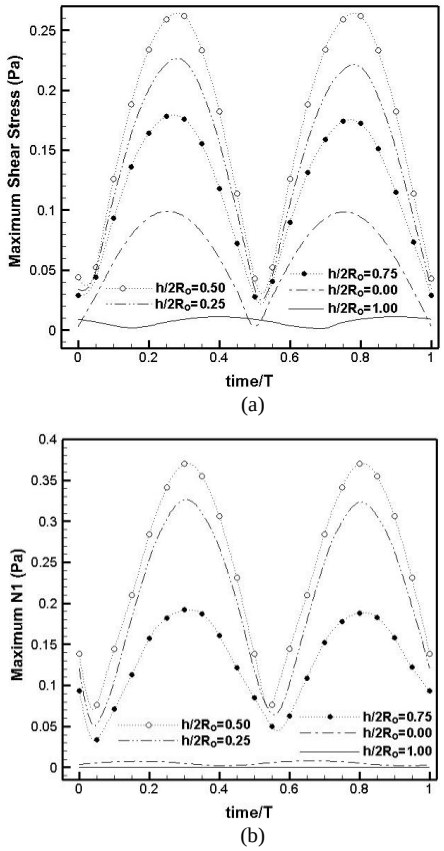

Figure 4. The time variations of the maximum value of (a) the shear stress and (b) the first normal stress difference (N_1) during one period for various $h/2R_o$ ratios at A=0.03 rad and ω=10 rad/sec.

Another interesting feature of the partially liquefied vitreous is the location of maximum shear and normal stresses during one period. It was found that for all $h/2R_o$ ratios in the range of (0, 1), the maximum stress components appear in the vicinity of interface and inside the vitreous gel region. Therefore, since the principal stress difference (PSD) consists of both first normal stress difference and shear stress (Eq. (4)), it is considered as a suitable parameter in order to interpret the stress contours and to illustrate the location of its maximum.

$$PSD = \sqrt{\left(\tau_{\theta\theta} - \tau_{rr}\right)^2 + 4\tau_{r\theta}^{\ 2}} = \sqrt{N_1^{\ 2} + 4\tau_{r\theta}^{\ 2}} \tag{4}$$

To this end, the PSD values were calculated for $h/2R_o$ ratios equal to 0 .25, 0.5 and 0.75 at a specific time (at which maximum stresses are appeared). As the Fig. 5 shows, in all three PVL fractions, the maximum values of PSD are formed on the equatorial plane in which the width of the cavity is maximum. From these contours, the maximum stresses are localized on the wall boundary, close to the interface and in the viscoelastic phase

portion. Also, the maximum PSD values vary in the range of 0.4 to 0.65 Pa as a function of $h/2R_o$ ratio.

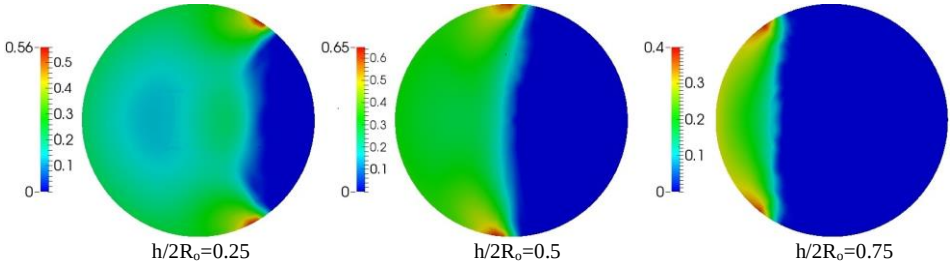

$h/2R_o$=0.25 $h/2R_o$=0.5 $h/2R_o$=0.75

Figure 5. The principal stress difference PSD (Pa) contours on the equatorial plane of vitreous chamber for ω=10 rad/sec, A=0.03 rad and different $h/2R_o$ ratios at time equal to 0.25T (the time of change in direction of motion).

In order to survey the details of the streamlines on the equatorial and vertical planes due to oscillatory motion, the numerical results for several $h/2R_o$ ratios in ω=10 rad/sec and A=0.03 rad are obtained at time equal to 0.25T (the time of change in direction of motion) and depicted in Fig. 6. In this figure, vitreous gel and liquefied vitreous regions have been shown with light and dark colors, respectively. It can be seen that, the flow fields of the PVL are appeared in the domain with almost symmetrical flow patterns. On the equatorial plane, parallel distributions of the curved streamlines are observed in both light and dark regions. Moreover, two main vortices are appeared in the liquefied vitreous gel portion of the vertical plane, and the circulating regions become stronger as $h/2R_o$ ratio increases. Notably, the velocity of the cavity boundary does not have any component in the vertical plane, so any secondary flow motion in this plane resembles the complex 3-D structure of the vitreous dynamic due to unsteady movements. Also, we found that these vortices grow in intensity with increasing amplitude of rotation which not reported here for sake of brevity. It is worth noting, the secondary flows might be an effective reason for the drug distribution in vertical directions of the PVL from fluid mechanical point of view, which requires more researches and have been left for future studies.

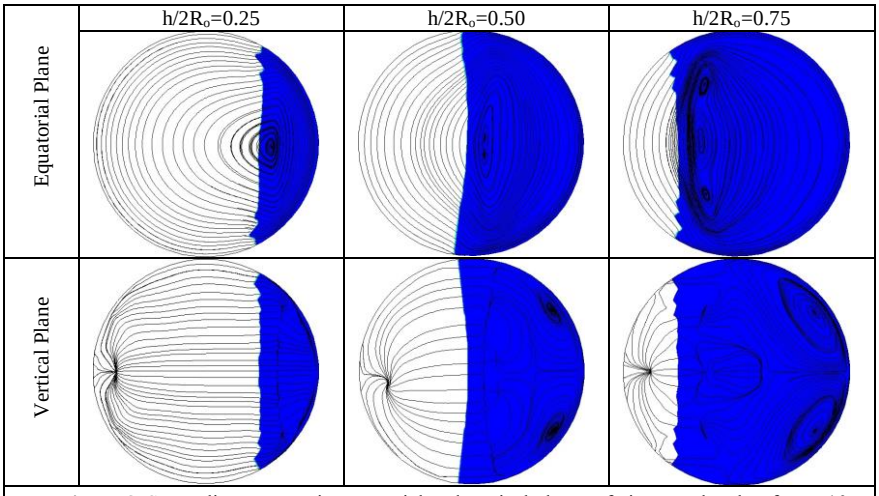

Figure 6. Streamline patterns in equatorial and vertical planes of vitreous chamber for ω=10 rad/sec, A=0.03 rad and different $h/2R_o$ ratios at time equal to 0.25T.

Finally, the maximum values of shear stress and first normal stress difference were obtained at various amplitudes of rotation for a specific PVL volume fraction ($h/2R_o$=0.5) and the results are shown in Fig. 7. The variations of the maximum N_1 are similar with maximum shear stress qualitatively, with these differences; the growth in maximum N_1 is more rapid than that for maximum shear stress, and also the range of maximum N_1 is one and half time higher. Moreover, this figure indicates that the variation with amplitude is non-linear so that increasing in amplitude of rotation from 0.03 to 0.3 rad leads to about 13 and 15 times increment in maximum shear stress and maximum N_1, respectively.

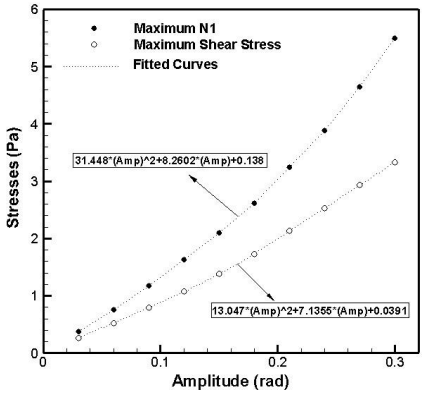

Figure 7. The variations of maximum shear stress and maximum first normal stress difference versus amplitude of rotation for angular frequency of 10 rad/sec in $h/2R_o$=0.5.

5. Conclusion

The main objective of the present work was to provide a reliable numerical procedure for studying the flow dynamics of partially liquefied vitreous humor as a two-phase viscoelastic-Newtonian fluid flow due to oscillatory motions. The developed numerical model was applied to investigate a PVL configuration with planar interface. The effects of various angular frequencies, amplitudes and volume fractions on the velocity field, shear stress, normal stress difference and streamline pattern were evaluated. The analysis of viscoelastic flow field revealed that using 3-modes Giesekus model for interpretation of artificial vitreous humor behavior as a gel-like substance has enough accuracy and acceptable consistency with provided rheological data in literature. It was found that when the volume fraction of the liquefied vitreous is higher, the secondary flow in the vertical plane of the PVL containing the interface layer becomes more noticeable which might be an effective reason for the enhanced drug dispersion, from fluid mechanics point of view. Also, in contrast to the normal and fully liquefied vitreous, the PVL generates normal stresses under the action of shear flow and the maximum normal stress difference can be more than the induced maximum shear stress. It was depicted that, the maximum shear and normal stresses depend on the volume fraction of liquefied vitreous region so that their maxima increase until $h/2R_o=0.5$ and then decrease again. These peaks of stresses occurred on the equatorial plane at the wall boundary near the interface and inside the vitreous region. Moreover, for $h/2R_o=0.5$ and angular frequency of 10 rad/sec, it was shown how the maximum shear stress varies in the range of [0.26-3.3] Pa and maximum normal stress difference changes from 0.37 to 5.5 with increase of the amplitude of rotation from 0.03 to 0.3 rad. It should be noted that the present research has some limits regarding to the real saccade movements in human eye. Firstly, the time variation of the saccade movements is not sinusoidal but this was assumed in present work as the first step for studying the complex phenomenon of the fluid dynamic for the partially liquefied vitreous. Secondly a spherical model was used for the vitreous chamber but the real shape is almost a sphere which has a deformation in one side due to the lens. Investigating the saccade movement effect for the real shape of the vitreous chamber when the virtuous gel is partially liquefied has been left for future studies.

6. Appendix. 1

The vitreous liquefaction usually originates from the central portion of the vitreous (Fig. A1, as early liquefaction). In this appendix, the analytical solution derived by David et al. [16] for single-phase viscoelastic fluid flow in a sphere is implemented for two-phase viscoelastic-Newtonian fluid flow (Fig. A1) and also it is utilized to validate the developed computational code.

The general analytic solution in the present work is similar to that obtained by David et al. as the geometry is the same but because of different boundary conditions regarding to our two-phase flow configuration the final solution is different.

By implementing oscillatory motion to low Reynolds number flow and neglecting the radial velocity component, pressure gradient, gravity and convective terms, the momentum equation in radial direction can be written as follow:

$$\frac{\partial u_\varphi(r)}{\partial t}=\frac{\eta^*}{\rho}\left[\frac{1}{r^2}\frac{\partial}{\partial r}\left(r^2\frac{\partial u_\varphi(r)}{\partial r}\right)\right]-\frac{u_\varphi(r)}{r^2\sin(\theta)} \tag{A1}$$

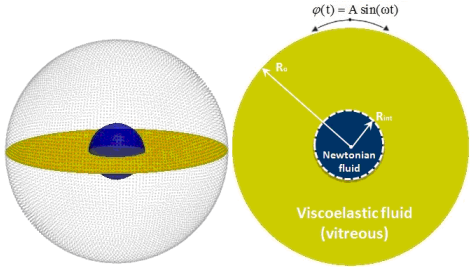

(a) (b) equatorial plane

Figure A1. The interface condition with the initial concentric spherical configuration of the partial vitreous liquefaction; vitreous gel and liquefied vitreous regions are shown in yellow and blue, respectively; (a) the computational model of the PVL, and (b) cross section along the equatorial plane of the model.

In the above equation, θ is the polar angle, the angle from the north pole of the model so that $\theta=\pi/2$ denotes the equatorial plane, also η^* is complex viscosity defined as [16]:

$$\eta^*=\frac{G^*}{i\omega}=\frac{G''}{\omega}-i\frac{G'}{\omega} \tag{A2}$$

The non-dimensional form of Eq. (A1) is obtained by introducing $R=r/R_o$ and $u_\varphi(r)/(AR_o\omega)=f(R)e^{i\omega t}\sin(\theta)$ as follow:

$$R^2f''+2Rf'-f\left(2+\frac{R^2R_o\rho\omega i}{\eta^*(=or\ \eta)}\right)=0 \tag{A3}$$

By substituting $\alpha^*=\sqrt{\rho\omega R_o^2/\eta^*}$ (the complex Womersley number), $\alpha=\sqrt{\rho\omega R_o^2/\eta}$ (the Womersley number), and $z=i^{1/2}R\alpha^*$ (=or α) into Eq. (A3), the modified spherical Bessel function of order 1 can be described as;

$$z^2f''+2zf'-f\left(2+z^2\right)=0 \tag{A4}$$

The system of general Bessel solution by assuming small amplitude oscillation for two-phase flow are expressed as:

$$f_1(z)=\left[C_1J_{3/2}(iz)+C_2Y_{3/2}(iz)\right]/\sqrt{z} \qquad R_{int}>r\geq 0 \tag{A5}$$

$$f_2(z)=\left[C_3J_{3/2}(iz)+C_4Y_{3/2}(iz)\right]/\sqrt{z} \qquad R_o>r\geq R_{int} \tag{A6}$$

In the above equation J and Y denote the first and second kind of modified spherical Bessel' function. Also the above solutions can be written as:

$$f_1(z)=\left[C_5\left(-\sinh z+z\cosh z\right)+C_6\left(\cosh z-z\sinh z\right)\right]/z^2$$

$$R_{int}>r\geq 0 \tag{A7}$$

$$f_2(z)=\left[C_7\left(-\sinh z+z\cosh z\right)+C_8\left(\cosh z-z\sinh z\right)\right]/z^2$$

$$R_o>r\geq R_{int} \tag{A8}$$

The constants C_1 to C_4 (or C_5 to C_8) are calculated by applying four boundary conditions as: (1) bounded velocity at centre of sphere, (2) no-slip condition at wall boundary, (3 and 4) continuous shear stress and its gradient across the interface. These constants were not reported here for sake of brevity. It should be noted that ignoring the surface tension, pressure

gradient and the radial velocity component, the two latest conditions represent the kinematic and dynamic boundary conditions at the interface, respectively (White and Corfield [45]). The introduced analytical solution was derived for the linear viscoelastic regime.

Since time=0.5T and T in sinusoidal periodic motion correspond to maximum velocity (minimum acceleration) and time=0.25T and 0.75T correspond to changing the direction of rotation and abrupt variation of the acceleration, thus we select these specific times for comparison the variations of tangential velocity magnitude (Fig. A2a) and shear stress magnitude (Fig. A2b) with respect to radius on the equatorial plane. Notably, the Fig. A2 is obtained for amplitude of 0.03 rad by considering various angular frequencies in the range of 3-10 rad/sec and different PVL volume fractions. According to these profiles, the excellent agreements between numerical results and introduced analytical solution are observed, confirming that the present numerical model well describes the behavior of the vitreous humor with different PVL fractions under oscillatory forcing.

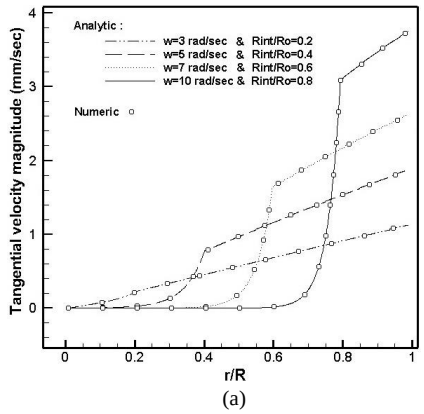

Figure A2. Comparisons of (a) tangential velocity magnitude at t=T (the profiles at t=0.5T are the same) (b) shear stress magnitude at t=0.25T (the profiles at t=0.75T are the same) between analytical and numerical results by considering amplitude equal to 0.03 rad, several angular frequencies and various volume fractions for the concentric PVL configuration.

7. References

1. Friedrich S., Cheng Y., Saville B., 1997, Finite elementmodeling of drug distribution in the vitreous humor of the rabbit eye, Annals of Biomedical Engineering, 25:303–314.
2. Kathawate J. and Acharya S., 2008, Computational modeling of intravitreal drug delivery in the vitreous chamber with different vitreous substitutes, International Journal of Heat and Mass Transfer, 51(23-24): 5598-5609.
3. Lee B., Litt M., Buchsbaum G., 1992, Rheology of the vitreous body, Part I: viscoelasticity of human vitreous. Biorheology, 29(5-6): 521-533.
4. Nickerson C.S., Park J., Kornfield J.A., Karageozian H., 2008, Rheological properties of the vitreous and the role of hyaluronic acid, Journal of biomechanics, 41(9):1840-1846.
5. Swindle K.E., Hamilton P.D., Ravi N., 2008, In situ formation of hydrogels as vitreous substitutes: Viscoelastic comparison to porcine vitreous, Journal of Biomedical Materials Research, Part A, Vol. 87A: 656-65.
6. Sharif-Kashani P., Hubschman J.P., Sassoon D., Kavehpour H.P., 2011, Rheology of the vitreous gel: effects of macromolecule organization on the viscoelastic properties. Journal of biomechanics 44(3): 419-423.
7. Piccirelli M., 2011, MRI of the Orbit during Eye Movement, Doctoral dissertation, ETH Zurich.
8. Rossi T., Querzoli G., Pasqualitto G., Iossa M., Placentino L., Repetto R., Stocchino A., Ripandelli G., 2012, Ultrasound imaging velocimetry of the human vitreous, Experimental eye research, 99: 98-104.
9. Bonfiglio A., Lagazzo A., Repetto R., Stocchino A., 2015, An experimental model of vitreous motion induced by eye rotations, Eye and Vision 2(1): 10.
10. Sebag J., 1987, Age-related changes in human vitreous structure. Graefe's archive for clinical and experimental ophthalmology, 225(2): 89-93.
11. Asaria R.H.Y. and Gregor Z.J. ,2002, Simple retinal detachments: identifying the at-risk case, Eye, 16(4) :404.
12. Balazs E.A. and Flood M.T., 1978, Age-related changes in the physical and chemical state of human vitreous, Third International Congress for Eye Research, Osaka, Japan.
13. Balazs E.A. and Denlinger J.L., 1982, Aging changes in the vitreus, in Aging and Human Visual Function, Alan R. Liss, New York, 45-57.
14. Takahashi K., Arai K., Hayashi S., Tanaka Y., 2006, Degree of degraded proteoglycan in human vitreous and the influence of peroxidation, Nippon Ganka Gakkai Zasshi, 110(3): 171-179.
15. Zhang Q., Filas B.A., Roth R., Heuser J., Ma N., Sharma S., ... & Shui Y.B., 2014, Preservation of the structure of enzymatically-degraded bovine vitreous using synthetic proteoglycan mimics, Investigative ophthalmology & visual science, 55(12): 8153-8162.
16. David T., Smye S., Dabbs T., James T., 1998, A model for the fluid motion of vitreous humour of the human eye during saccadic movement, Physics in Medicine & Biology 43(6): 1385.
17. Lee E., Lee Y.H., Pai Y.T., Hsu J.P., 2002, Flow of a viscoelastic shear-thinning fluid between two concentric rotating spheres, Chemical Engineering Science, 57(3): 507-514.
18. Meskauskas J., Repetto R., Siggers J.H., 2011, Oscillatory motion of a viscoelastic fluid within a spherical cavity, Journal of Fluid Mechanics, 685: 1-22.
19. Repetto R., Tatone A., Testa A., Colangeli E., 2011, Traction on the retina induced by saccadic eye movements in the presence of posterior vitreous detachment, Biomechanics and modeling in mechanobiology, 10(2): 191-202.
20. Abouali O., Modareszadeh A., Ghaffariyeh A., Tu J., 2012, Numerical simulation of the fluid dynamics in vitreous cavity due to saccadic eye movement, Medical engineering & physics, 34(6): 681-692.

21. Modareszadeh A. and Abouali O., 2014, Numerical simulation for unsteady motions of the human vitreous humor as a viscoelastic substance in linear and non-linear regimes, Journal of Non-Newtonian Fluid Mechanics 204: 22-31.
22. Eisner G., 1975, Zur anatomie des glaskörpers. Albrecht von Graefes Archiv für klinische und experimentelle Ophthalmologie, 193(1): 33-56.
23. Tolentino F.I., Schepens C.L., Freeman H.M., 1975, Vitreoretinal Disorders 121-129. Philadelphia, Pa: WB Saunders Co.
24. Sebag J. and Balazs E.A., 1984 Pathogenesis of cystoid macular edema: an anatomic consideration of vitreoretinal adhesions, Survey of ophthalmology, 28: 493-498.
25. Kishi S. and Shimizu K., 1990, Posterior precortical vitreous pocket. Archives of Ophthalmology, 108(7): 979-982.
26. Sebag J., 1987, Age-related changes in human vitreous structure. Graefe's archive for clinical and experimental ophthalmology, 225(2): 89-93.
27. Kummer M.P., Abbott J.J., Dinser S., Nelson B.J., 2007, Artificial vitreous humor for in vitro experiments. In Engineering in Medicine and Biology Society, 29th Annual International Conference of the IEEE, 6406-6409.
28. Macosko C.W., 1994, Rheology: principles, measurements and applications. New York: VCH Publishers.
29. Giesekus H., 1982, A simple constitutive equation for polymer fluids based on the concept of deformation-dependent tensorial mobility. Journal of Non-Newtonian Fluid Mechanics, 11(1-2): 69-109.
30. Hirt C.W. and Nichols B.D., 1981, Volume of fluid (VOF) method for the dynamics of free boundaries. Journal of computational physics, 39(1): 201-225.
31. Rusche H., 2003, Computational fluid dynamics of dispersed two-phase flows at high phase fractions, Doctoral dissertation, Imperial College London, University of London.
32. Benson D.J., 2002, Volume of fluid interface reconstruction methods for multi-material problems, Applied Mechanics Reviews, 55(2): 151-165.
33. Piro D.J. and Maki K.J., 2013, An adaptive interface compression method for water entry and exit, University of Michigan.
34. Weller H.G., Tabor G., Jasak H., Fureby C., 1998, A tensorial approach to computational continuum mechanics using object-oriented techniques. Computers in physics, 12(6): 620-631.
35. Patankar S., 1980, Numerical Heat Transfer and Fluid Flow, Series in computational and physical processes in mechanics and thermal sciences, Hemisphere Publishing Company, ISBN 9780891165224
36. Versteeg H.K. and Malalasekera W., 2007, An introduction to computional fluid dynamics: The finite volume method.
37. Issa R.I., 1985, Solution of the implicitly discretised fluid flow equations by operator-splitting, J. Comput. Phys. 62: 40-65.
38. Ferziger J.H. and Peric M., 2012, Computational methods for fluid dynamics. Springer Science & Business Media, third edition.
39. Damián S.M., 2013, An extended mixture model for the simultaneous treatment of short and long scale interfaces, Doktorarbeit, Universidad Nacional Del Litoral, Facultad de Ingenieria y Ciencias Hidricas.
40. Jasak H., Weller H.G., Gosman A.D., 1999, High resolution NVD differencing scheme for arbitrarily unstructured meshes, International journal for numerical methods in fluids, 31(2): 431-449.
41. Ajiz M.A. and Jennings A. ,1984, A robust incomplete Choleski-conjugate gradient algorithm, International Journal for numerical methods in engineering, 20(5): 949-966.
42. Lee J., Zhang J., Lu C.C., 2003, Incomplete LU preconditioning for large scale dense complex linear systems from electromagnetic wave scattering problems, Journal of Computational Physics, 185(1): 158-175.
43. Habla F., Obermeier A., Hinrichsen O., 2013, Semi-implicit stress formulation for viscoelastic models: Application to three-dimensional contraction flows, Journal of Non-Newtonian Fluid Mechanics, 199: 70-79.
44. Guénette R. and Fortin M., 1995, A new mixed finite element method for computing viscoelastic flows, Journal of non-newtonian fluid mechanics, 60(1): 27-52.
45. White F.M. and Corfield I., 1974, Viscous fluid flow, vol. 3.